Analytical Approach to THD Formulation and Optimization in Sine-PWM-Based Single-Phase Multilevel Inverters With Variable DC Ratios

Eli Barbie, Mor Mordechai Peretz, *Member, IEEE*, Alon Kuperman, *Senior Member, IEEE*, and Dmitry Baimel, *Senior Member, IEEE*

***Abstract*— Asymmetric multilevel inverters (MLIs) with unequal voltage steps (UVSs) are often combined with the staircase modulation (SCM) technique to improve both voltage and current total harmonic distortion (THD) – an approach known as optimal minimization of THD (OMTHD). This is usually achieved by varying both the switching angles (SAs) and the dc source ratios (DCR), to obtain the desired modulation index (MI) while THD is minimized. In this article, a novel sine pulsewidth modulation (SPWM) based OMTHD is considered as an alternative to SCM-based OMTHD. Because only the DCRs need to be optimized instead of both SAs and DCRs, the OMTHD process is simplified, while voltage THD, current THD, as well as power efficiency, are improved, especially for the medium-low MI range, compared to conventional SPWM. An analytical formulation of phase-voltage THD for UVS-based SPWM MLIs is derived and utilized for the novel SPWM-based OMTHD. Validation is carried out by theoretical analysis, digital simulations, and real-time controller + Hardware-in-Loop (C-HIL)-based experiments.**

***Index Terms*— Level-shifted (LS), multilevel inverters (MLIs), optimization, sine pulsewidth modulation (SPWM), total harmonic distortion (THD), unequal dc sources.**

I. Introduction

MULTILEVEL inverters (MLIs) hold immense importance in modern electric power conversion applications while they keep gaining more popularity within the industrial and research communities, especially with applications that demand high-quality output voltage waveforms [1], [2], [3], [4], [5], [6].

MLIs can be supplied with equal dc sources, and thus, generate waveforms with equal voltage steps (EVSs) [6]. MLIs, particularly of the M-cell cascaded H-bridge (CHB) topology, can also be supplied with unequal dc sources, which may be done to maximize the number of voltage levels (N) up to $N = 3^M$ or to lower the total harmonic distortion (THD) by generating waveforms of unequal voltage steps (UVSs) with $N = 2M + 1$ (N is odd for CHB) [6], [7], [8], [9], [10].

Achieving the desired modulation index (MI) while minimizing the voltage or current THD, is the main objective of any MLI operation [7], [9]. While the majority of power conversion applications utilize conventional EVS-based MLIs, UVS-based MLIs are becoming more popular in some niche applications that demand low THD across the entire MI range [7], [9]. Until now, UVS-based MLIs, such as asymmetrical CHBs, were only operated using fundamental-frequency-based switching strategies, generally referred to as staircase modulation (SCM) switching [7]. To better utilize UVS-based MLIs, the SCM strategy is traditionally combined with a THD [or Weighted THD (WTHD)] optimization technique, known as optimal minimization of THD (OMTHD), in which both the switching angles (SAs) and the dc source ratios (DCRs) are precalculated by minimizing a multiobjective function, given a target MI [7].

The main limitation of SCM-based OMTHD is that adequate THD values cannot be obtained for the low MI range unless bulky and expensive MLIs with $N \geq 7$ are employed [7], [11]. The proximity between the fundamental and the switching frequencies in SCM increases the size of the output filters, which in turn, increases cost and limits dynamic performance [9]. The more popular high switching frequency-based approaches, such as the sine pulsewidth modulation (SPWM) [12], [13], [14], [15], [16], [17], [18], [19], [20] provide better dynamic performance, especially for low-cost MLIs with $N < 7$ [6], [7], [9]. Moreover, neutral-point-clamped (NPC) based MLIs, which rely on MLI-side voltage balancing control schemes, and therefore, are incompatible with SCM techniques, can also be used with the proposed SPWM-based OMTHD, provided that active frontend solutions, such as the multilevel rectifier (MLR) introduced in [8], are utilized [9], [11].

Unlike SCM-based switching strategies where analytical formulations of THD are feasible and readily available due to the simplicity of the staircase waveforms [7], for multilevel SPWM, THD is traditionally calculated by spectra-based numerical approximations, accounting for up to 50 harmonics, as per IEEE 519 standard recommendations [21], [22]. Such an approach cannot be used for practical THD optimization and is subject to a significant amount of underestimation errors [22].

There are two main SPWM techniques: 1) level-shifted (LS) SPWM [14], [19], in which the source signal is segregated

Manuscript received 30 June 2022; revised 22 September 2022; accepted 1 November 2022. Date of publication 7 November 2022; date of current version 13 June 2023. This work was supported in part by the Israel Science Foundation under Grant 2186/19 and in part by the Israel Ministry of Energy. Recommended for publication by Associate Editor Josep Pou. *(Corresponding author: Dmitry Baimel.)*

Eli Barbie and Dmitry Baimel are with the Department of Electrical and Electronics Engineering, Shamoon College of Engineering, Beer Sheva 8410802, Israel (e-mail: barbie@post.bgu.ac.il; baimel@sce.ac.il).

Mor Mordechai Peretz and Alon Kuperman are with the School of Electrical and Computer Engineering, Ben-Gurion University of the Negev, Beer Sheva 84105, Israel (e-mail: morp@post.bgu.ac.il; alonk@bgu.ac.il).

This article has supplementary material provided by the authors and color versions of one or more figures available at https://doi.org/10.1109/JESTPE.2022.3220576.

Digital Object Identifier 10.1109/JESTPE.2022.3220576

vertically by utilizing a total of $N-1$ LS carriers and 2) phase-shifted (PS) SPWM [13], [16], in which the source signal is segregated horizontally (in time) by utilizing a total of $N-1$ carriers, which are shifted by $360°/(N-1)$ (carrier period degrees) [15]. While LS-SPWM is very simple to implement, it has the disadvantage of unequal power sharing between the MLI's components [16]. The PS-SPWM solves the power-sharing problem [19], but sacrifices switching losses and current THD in MLIs with a lower value of N [9], [13].

Successive THD optimization relies on accurate THD formulation [7]. An analytical approach to asymptotic phase-voltage SPWM THD calculation was first suggested in [22] as a form of a piecewise recursive expression, valid only for conventional EVS-based SPWM MLIs with odd values of N, thus, cannot be utilized for SPWM-based OMTHD, which requires a UVS-based MLI.

The two main objectives of this work are as follows: 1) to derive a generic closed-form THD expression for UVS- and EVS-based SPWM of both odd and even values of N and 2) to apply the OMTHD strategy to SPWM-based switching technique using the derived expression.

The proposed novelties are verified by simulations and controller + Hardware-in-Loop (C-HIL) based experimental validations, using a CHB-based MLI example. The Supplementary Materials, containing Maple and MATLAB implementations of the THD function, and precalculated sets of optimum DCRs for different values of N ($4 \le N \le 11$) are also provided as a downloadable file. The main contributions of this research are as follows:

1) The novel analytical THD formulation eliminates the need for inaccurate numerical THD approximations in SPWM MLIs of any topology.
2) Not only that voltage and current THD are significantly reduced in the proposed SPWM-based OMTHD, but power-sharing variability and switching losses are also improved over conventional SPWM techniques.
3) The simplified novel OMTHD eliminates the need for a complex multiobjective fitness function, thus preventing suboptimal results due to difficulty in choosing the scalarization weights [7].
4) The SPWM-based OMTHD may benefit applications that share a point of common coupling (PCC) between the MLI and multiple loads, such as renewable energy to grid interfaces, which may be adversely affected by the nonoptimal voltage and current quality [7], [21].
5) The proposed methodology can later be expanded to allow line-voltage THD to better suit three-phase MLIs [7].

The rest of this article is organized as follows. First, an analytical closed-form UVS-compatible expression of phase-voltage THD in LS SPWM-based MLIs is derived in Section II. Then, in Section III, the revealed formulation is utilized to obtain a novel SPWM-based OMTHD for UVS-capable MLIs, by utilizing a simple single-objective fitness function, while some theoretical results are presented and discussed to highlight the difference between conventional EVS-based SPWM strategies and the novel UVS-based SPWM strategy. Finally, in Section IV, the proposed novelties are thoroughly verified, and this article is concluded in Section V.

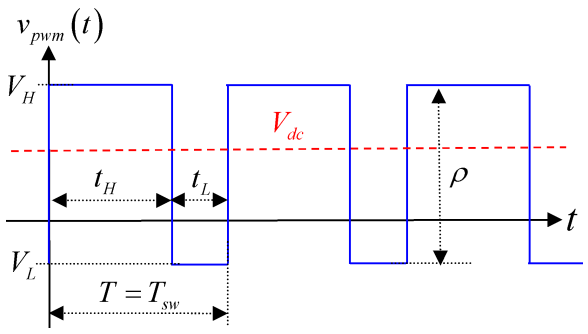

Fig. 1. Generic PWM waveform.

II. Analytical SPWM THD Expression

Since the horizontally segregated PS-SPWM cannot take advantage of a UVS-capable MLI, thus, leaving no room for optimization, the proposed SPWM-based OMTHD utilizes the LS-SPWM approach. While the revealed asymptotic THD formulation is derived under the assumption that the switching frequency is infinitely high, it can still be practically applied to MLIs with switching frequencies only 21 times higher than the fundamental frequency [22].

A. AC Ripple of a PWM Waveform

The %-THD of a PWM voltage, $v_{\text{pwm}}(t)$, may be defined as the ratio between the effective value of the ac component, $V_{\text{rms}}^{\text{ac}}$, which represents the root mean square (rms) of all unwanted harmonics (ripple) and the effective (rms) value of the fundamental component, V_1 of the PWM waveform, vis,

$$\text{THD} = 100 \cdot \frac{\sqrt{2}V_{\text{rms}}^{\text{ac}}}{V_1}. \tag{1}$$

The effective value of the ac ripple can be indirectly calculated using the values of the total rms and the dc components as

$$V_{\text{rms}}^{\text{ac}} = \sqrt{V_{\text{rms}}^2 - V_{\text{dc}}^2} \tag{2}$$

where the squared average (dc) V_{dc}^2 and the squared total rms components are given by the following equations:

$$V_{\text{dc}}^2 = \left(\int_0^T v_{\text{pwm}}(t)dt\right)^2 \tag{3}$$

$$V_{\text{rms}}^2 = \int_0^T v_{\text{pwm}}^2(t)dt. \tag{4}$$

Fig. 1 illustrates a generic PWM signal with a switching period of T_{sw} ($1/f_{\text{sw}}$) and its modulated average value (assuming slow varying source signal). Graphically applying (3) and (4) to the generic PWM waveform of Fig. 1, while utilizing the duty cycle notations: $d = t_H/T_{\text{sw}}$ and $1-d = t_L/T_{\text{sw}}$, there is

$$V_{\text{dc}}^2 = (V_L + (V_H - V_L)d)^2 \tag{5}$$

$$V_{\text{rms}}^2 = V_L^2 + \left(V_H^2 - V_L^2\right)d. \tag{6}$$

Combining (4) and (5) with (2) and using the PWM's magnitude notation, $\rho = V_H - V_L$, the ac ripple is obtained

$$V_{\text{rms}}^{\text{ac}} = \rho\sqrt{(1-d)d}. \tag{7}$$

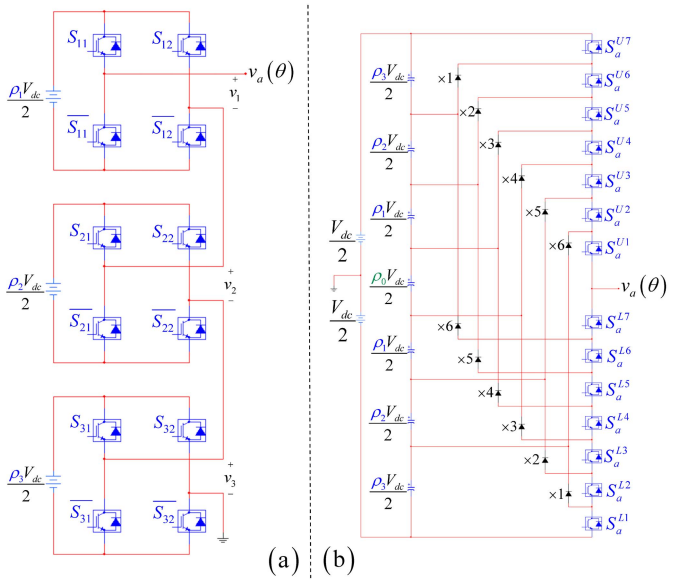

Fig. 2. Schematics of N-level UVS-capable MLI phase-legs. (a) Seven-level CHB (odd-N example). (b) Eight-level NPC (even-N example).

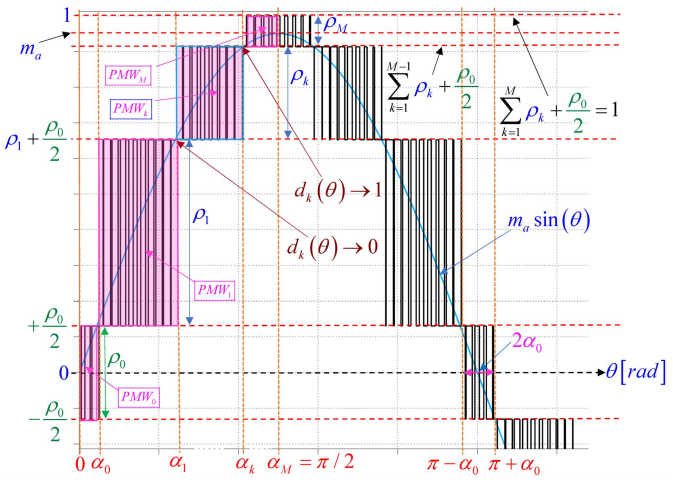

Fig. 3. Normalized generic N-level (M_ρ-section) UVS-based LS SPWM waveform of odd symmetry.

B. UVS-Based MLIs With LS SPWM

Consider an N-level UVS/EVS-compatible CHB MLI phase-leg, where N is odd (i.e., $N = 7$), and an NPC MLI, where N is even (i.e., $N = 8$), as depicted in Fig. 2(a) and (b), respectively. Such generalized topologies share the same dc supply voltage, denoted as $V_{\rm dc}$, so each phase leg may output an ac voltage at a range of $\pm V_{\rm dc}$/2p-p. Assuming LS-SPWM operation, then, the phase-voltage output can be represented as a normalized (scaled by $2/V_{\rm dc}$) waveform with quarter-wave odd-symmetry, as depicted in Fig. 3. The waveform consists of M partial modulation window (PMW) sections per quarter-wave, each with a height of ρ_k, plus an optional half-section at the origin with a height of $\rho_0/2$, in case N is even (see Fig. 2), where M is generally related to N (odd or even) as

$$M = \left\lfloor \frac{N-1}{2} \right\rfloor \tag{8}$$

where $\lfloor\,\rfloor$ denotes the floor operator [7]. The kth PMW's (PMW$_k$) height, ρ_k, presents the ρ_k DCR value. The transition from any two consecutive PMW sections, namely, from PMW$_{k-1}$ to PMW$_k$, is assumed to occur at an SA of α_{k-1}. This means that each kth PMW, with a height of ρ_k, begins at α_{k-1} and ends at α_k, as illustrated by Fig. 3, where $k = 0, 1, 2, \ldots, M$. This way, in the case where N is odd, therefore PMW$_0$ is absent, there is $\alpha_0 = 0$ and $\rho_0 = 0$. Note that the width of PMW$_0$ is α_0 and $\alpha_M = \pi/2$ always.

The DCR set, $\rho = \{\rho_0, \rho_1, \ldots, \rho_k, \ldots, \rho_M\}$, determines the magnitude of each PMW section, as well as the height of the MLI's phase voltage step (see Fig. 2). The DCRs, are given in per-unit (p.u.) where the total number of DCRs, M_ρ, (PMW sections), including the optional one at the origin, ρ_0, for even N values, can be expressed as

$$M_\rho = \left\lfloor \frac{N}{2} \right\rfloor. \tag{9}$$

The EVS-based arrangement is also possible by the following substitution [7] (see Figs. 2(b) and 3)

$$\rho_0 = \rho_1 = \rho_2 = \cdots = \rho_k = \frac{2}{N-1}. \tag{10}$$

Note that the DCRs are normalized for both EVS and UVS configurations, namely

$$\sum_{k=1}^{M} \rho_k + f_T \rho_0 = 1, \quad 0 \le \rho \le 1 \tag{11}$$

where f_T serves as a parity toggle function [7], defined as

$$f_T = \left\lfloor \frac{N}{2} \right\rfloor - \frac{N-1}{2} = \begin{cases} 0, & \text{odd } N \\ \dfrac{1}{2}, & \text{even } N. \end{cases} \tag{12}$$

Using concepts previously derived in [7] for UVS-based SCM, a general expression for the kth SA, excluding the one at the origin, α_0, can be easily determined from Fig. 3 as

$$\alpha_k = \arcsin\left(\min\left(1, \frac{1}{m_a} \cdot \left(\sum_{i=1}^{k} \rho_i + \frac{\rho_0}{2}\right)\right)\right) \quad \text{with} \quad \begin{matrix} k = 0, 1, \ldots, M \\ 0 \le \alpha_k \le \pi/2. \end{matrix} \tag{13}$$

Therefore, α_0 is given as

$$\alpha_0 = \arcsin\left(\min\left(1, \frac{\rho_0}{2m_a}\right)\right). \tag{14}$$

Note that the max() operator ensures a real result of $\pi/2$ whenever the argument inside the arcsin() function exceeds unity. Assuming a single-edge, regularly sampled SPWM [9] with a sampling period similar to the switching period, namely

$$T_s = T_{\rm sw} = \frac{1}{f_{\rm sw}} \tag{15}$$

a zoomed-in section of the normalized N-level (M_ρ-section) UVS-based LS-SPWM waveform from Fig. 3 is depicted in Fig. 4, highlighting two consecutive PWM sections: the previous $(n-1)$th, and the current nth. This includes

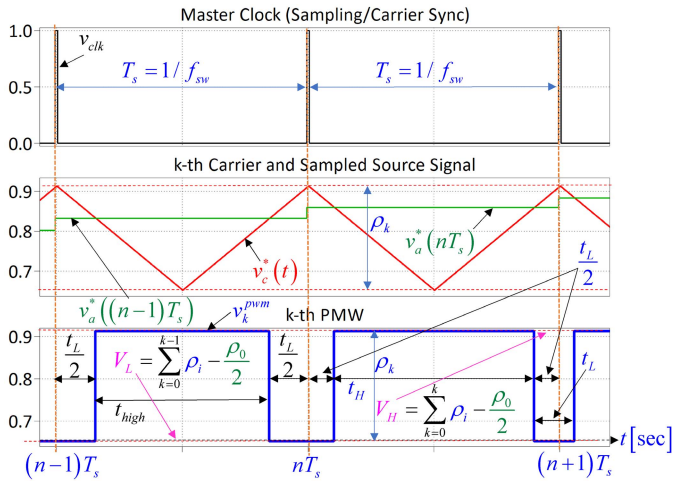

Fig. 4. Two generic consecutive PWM sections ($n-1$th and nth) of UVS-based SPWM.

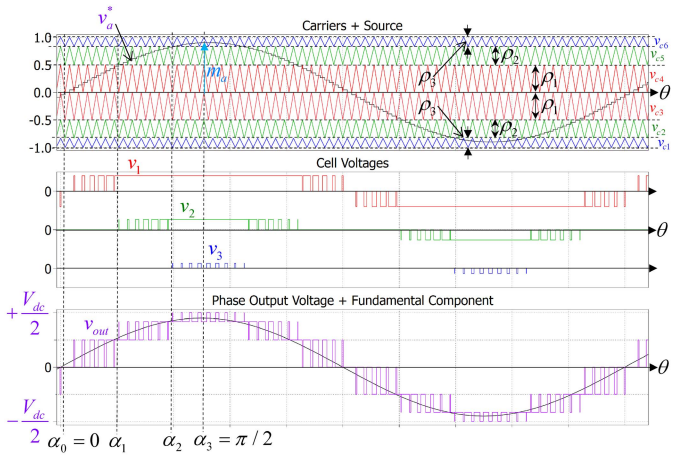

Fig. 5. Carrier signals, CHB's output cell voltages, and the total output voltage of a proposed seven-level UVS-based SPWM using the PD method.

(from top to bottom): the master clock (carrier synchronization), the sampled source signal (normalized sinewave), the carrier, and the resulting consecutive $(n-1)$th and nth PWM sections.

The modulated signal is assumed to take the following form:

$$v_a^* = m_a \sin(\theta) \quad 0 \le m_a \le 1 \tag{16}$$

where m_a is the MI, which is essentially the normalized magnitude of the desired fundamental component at a frequency of f_1, and $\theta = 2\pi f_1 t$ represents the electric angle.

A UVS-based LS-SPWM utilizing the simple phase disposition (PD) multicarrier pattern [13] is shown in Fig. 5 for $N = 7$ ($M = M_\rho = 3$), $m_a = 0.9$, and a DCR set of $\rho = [\rho_1, \rho_2, \rho_3] = (1/6) \cdot [3, 2, 1]$. Note that the DCR distribution of the proposed N-level UVS-based multicarriers must always utilize a symmetrical "smiley" arrangement, which can be generally defined as follows:

$$\rho_N = \rho_{f(k)}, \quad \left| \begin{array}{l} f(k) = \left\lceil \dfrac{|N-2k|}{2} \right\rceil \\ k = 1, 2, \ldots, N-1 \end{array} \right. \tag{17}$$

where $|\,|$ and $\lceil\,\rceil$ denotes the abs() and the ceiling() operators, respectively. For example, applying (17) with $N = 7$ and $N = 8$ leads to: $\{\rho_3, \rho_2, \rho_1, \rho_1, \rho_2, \rho_3\}$ and $\{\rho_3, \rho_2, \rho_1, \rho_0, \rho_1, \rho_2, \rho_3\}$, respectively (see Fig. 5).

C. Analytic SPWM Formulation

The desired THD expression should be an analytic function of N, m_a, and the DCR set, ρ. Using (1), the THD expression should be generally defined as follows:

$$\mathrm{THD}(N, m_a, \rho) = 100 \cdot \frac{\sqrt{2}\ V^{\mathrm{ac}}_{\mathrm{SPWM}}(N, m_a, \rho)}{m_a}. \tag{18}$$

Since all three function variables (the scalars N, m_a, and the array ρ), are mutually independent, the desired THD function (18) is only determined by the effective (rms) ac expression of the $V^{\mathrm{ac}}_{\mathrm{SPWM}}(N, m_a, \rho)$ (voltage ripple) waveform. The ac rms value of the kth PMW, shown in Fig. 4, can be obtained using the derived ac rms expression from (7), vis,

$$V^{\mathrm{ac}}_{\mathrm{pmw}(k)}(\theta) = \rho_k \sqrt{(1 - d_k(\theta)) d_k(\theta)}. \tag{19}$$

A duty ratio function (DRF), $d(\theta)$, is identified in Fig. 3 and expressed as a piecewise linear function source signal

$$d(\theta) = \begin{cases} d_0(\theta), & 0 \le \theta \le \alpha_0 \\ d_1(\theta), & \alpha_0 \le \theta \le \alpha_1 \\ \quad \vdots & \\ d_k(\theta), & \alpha_{k-1} \le \theta \le \alpha_k \\ \quad \vdots & \\ d_M(\theta), & \alpha_{M-1} \le \theta \le \end{cases} \qquad 0 \le \alpha_k \le \pi/2. \tag{20}$$

Using linear mapping, the DRF is utilized to rescale each kth PMW portion of the sampled source signal, $v_a^*(nT_s)$ from its original $v_a^*(\alpha_{k-1}) \le d_k(\theta) \le v_a^*(\alpha_k)$ range, toward a true duty ratio range of $0 \le d_k(\theta) \le 1$ (see Figs. 3 and 4), vis,

$$d_k(\theta) = m_k \cdot v_a^*(\theta) + n_k = m_k \cdot m_a \sin(\theta) + n_k \tag{21}$$

where the coefficients are obtained graphically using Fig. 3

$$m_k = \frac{1}{\rho_k}, \quad n_k = -\frac{1}{\rho_k}\left(\sum_{i=0}^{k-1} \rho_i - \frac{\rho_0}{2}\right). \tag{22}$$

Note that for the (optional) first (0th) PMW, (22) becomes

$$m_0 = \frac{1}{\rho_0}, \quad n_0 = \frac{1}{2}. \tag{23}$$

Combining (21) with (22), there is

$$d_k(\theta) = \frac{m_a \sin(\theta)}{\rho_k} - \frac{1}{\rho_k}\left(\sum_{i=0}^{k-1} \rho_i - \frac{\rho_0}{2}\right), \quad k = 0, 1, \ldots, M \tag{24}$$

where M is defined in (8). As Fig. 3 reveals, all PMW sections (PMW_k) occupy different nonoverlapping timeframes, thus they may be treated as mutually orthogonal functions of the electrical angle, θ, vis,

$$\int_0^{\pi/2} V^{\mathrm{ac}}_{\mathrm{pwm}(k)}(\theta) d\theta = 0.$$

This means that $V^{\mathrm{ac}}_{\mathrm{pwm}(k)}$ (19) can be utilized to obtain the total voltage ripple function, $V^{\mathrm{ac}}_{\mathrm{SPWM}}$, by applying (4) to $V^{\mathrm{ac}}_{\mathrm{pwm}(k)}$ over the fundamental period and taking the square root, vis,

$$V^{\mathrm{ac}}_{\mathrm{SPWM}} = \sqrt{\frac{2}{\pi}\int_0^{\pi/2}\left(V^{\mathrm{ac}}_{\mathrm{pwm}(k)}(\theta)\right)^2 d\theta}. \tag{25}$$

Combining (25), (19), and (24), and rearranging using Fig. 3 to identify the integration boundaries over a single PMW section ($\alpha_{k-1} \le \theta \le \alpha_k$), then taking summation to account for all sections, including the (optional) 0th PMW, there is

$$V^{\mathrm{ac}}_{\mathrm{SPWM}} = \sqrt{\frac{2}{\pi}\sum_{k=1}^{M}\int_{\alpha_{k-1}}^{\alpha_k}\left(\begin{pmatrix} m_a\sin(\theta) - \sum_{i=0}^{k-1}\rho_i + \frac{\rho_0}{2}\end{pmatrix}\cdot\left(\sum_{i=0}^{k}\rho_i - \frac{\rho_0}{2} - m_a\sin(\theta)\right)\right)d\theta + \left(V^{\mathrm{ac}}_{\mathrm{pmw}(0)}\right)^2}$$

where $V^{\mathrm{ac}}_{\mathrm{pmw}(0)}$ can be obtained using (19), (21), and (23). Once the integral is symbolically evaluated, the above terms are combined along with (8) and simplified, and the 0th DCR, $\rho_0$is substituted by $2f_T$, according to (12), the final generic closed-form total voltage ripple function from (18) is obtained as, equation (26), shown at the bottom of the page, where α_k and α_{k-1} are obtained from (12) and (13), as

$$\alpha_k = \arcsin\left(\min\left(1, \frac{1}{m_a}\cdot\left(\sum_{i=1}^{k}\rho_i + f_T\rho_0\right)\right)\right)$$
$$\alpha_{k-1} = \arcsin\left(\min\left(1, \frac{1}{m_a}\cdot\left(\sum_{i=1}^{k-1}\rho_i + f_T\rho_0\right)\right)\right). \tag{27}$$

The final generic THD expression is therefore formulated by combining (26), and (27) with (18), using (12), resulting in a true closed-form expression of N, m_a, and ρ.

D. THD Expressions of Special Simplified Cases

For the more common MLIs with only odd values of N, such as CHBs, the proposed THD expression may be simplified by setting f_T to 0, combining (18) with (26) and (27), then rearranging, which leads to the simplified and compact expression, given by (28), as shown at the bottom of the page.

$$V^{\mathrm{ac}}_{\mathrm{SPWM}} = \sqrt{\frac{2m_a}{\pi}\sum_{k=1}^{\lfloor\frac{N-1}{2}\rfloor}\left(\begin{pmatrix}(\cos(\alpha_{k-1}) - \cos(\alpha_k))\cdot\left(\sum_{i=1}^{k}\rho_i + \sum_{i=0}^{k-1}\rho_i\right)\\ -\left(\frac{\alpha_k-\alpha_{k-1}}{m_a}\right)\cdot\left(\begin{pmatrix}\left(\sum_{i=0}^{k}\rho_i - f_T\rho_0\right)\cdot\left(\sum_{i=0}^{k-1}\rho_i - f_T\rho_0\right)\\ +\frac{m_a^2}{2}\end{pmatrix}\right)\end{pmatrix} + \frac{1}{\pi}\cdot\begin{pmatrix}\min(m_a, f_T\rho_0)\sqrt{m_a^2 - \min(m_a, f_T\rho_0)^2}\\ +\left(2(f_T\rho_0)^2 - m_a^2\right)\arcsin\left(\min\left(1, \frac{f_T\rho_0}{m_a}\right)\right)\end{pmatrix} - \frac{m_a^2}{2\pi}\sin(2\alpha_0)} \tag{26}$$

$$\mathrm{THD}(N, m_a, \rho) = \frac{100}{m_a}\cdot\sqrt{\frac{4}{\pi}\sum_{k=1}^{\frac{N-1}{2}}\left(\begin{pmatrix}\sqrt{1 - \min\left(1, \frac{1}{m_a}\sum_{i=1}^{k-1}\rho_i\right)^2}\\ -\sqrt{1 - \min\left(1, \frac{1}{m_a}\sum_{i=1}^{k}\rho_i\right)^2}\end{pmatrix}\cdot\left(\sum_{i=1}^{k}\rho_i + \sum_{i=1}^{k-1}\rho_i\right)\cdot m_a + \begin{pmatrix}\arcsin\left(\min\left(1, \frac{1}{m_a}\sum_{i=1}^{k-1}\rho_i\right)\right)\\ -\arcsin\left(\min\left(1, \frac{1}{m_a}\sum_{i=1}^{k}\rho_i\right)\right)\end{pmatrix}\cdot\begin{pmatrix}\left(\sum_{i=1}^{k}\rho_i\right)\cdot\left(\sum_{i=1}^{k-1}\rho_i\right)\\ +\frac{m_a^2}{2}\end{pmatrix}\right)} \tag{28}$$

$$\mathrm{THD}(N, m_a) = \frac{100}{m_a}\cdot\sqrt{\frac{8}{\pi}\sum_{k=1}^{\frac{N-1}{2}}\left(\begin{pmatrix}m_a\cdot\begin{pmatrix}\sqrt{1 - \min\left(1, \frac{2(k-1)}{m_a\cdot(N-1)}\right)^2}\\ -\sqrt{1 - \min\left(1, \frac{2k}{m_a\cdot(N-1)}\right)^2}\end{pmatrix}\cdot\frac{2k-1}{N-1}\\ +\begin{pmatrix}\arcsin\left(\min\left(1, \frac{2(k-1)}{m_a\cdot(N-1)}\right)\right)\\ -\arcsin\left(\min\left(1, \frac{2k}{m_a\cdot(N-1)}\right)\right)\end{pmatrix}\cdot\begin{pmatrix}\frac{2k\cdot(k-1)}{(N-1)^2}\\ +\frac{m_a^2}{4}\end{pmatrix}\end{pmatrix}} \tag{29}$$

Furthermore, by combining (28) with (10), and rearranging, an even more simplified EVS-based THD expression for odd-N values is obtained, which is given by (29), as shown at the bottom of the previous page. It should be indicated that the THD expression in (29) is mathematically equivalent to the proposed piecewise expression in [22].

III. Proposed SPWM OMTHD

A. Optimization Problem Definition

The OMTHD objective is to calculate the optimum design variables – the DCRs, in this case, to obtain a minimum THD given the desired MI value. Since in SPWM the MI is independent of the DCR variables, the optimization problem can be made simple by utilizing a single-objective fitness function – the THD expression from (18). The fitness function must be solved for the optimum DCRs (the design variables), given the values of the parameters N and m_a, where m_a becomes an independent variable (the desired MI value), denoted here as m_T

$$\begin{aligned} &\text{min: } \mathrm{THD}(N, m_a, \rho) \\ &\text{s.t. } \begin{cases} \text{a}), & m_a = m_T \\ \text{b}), & \displaystyle\sum_{k=1}^{M} \rho_k + f_T \rho_0 = 1 \\ \text{c}), & 0 \le \rho_k \le 1 \\ \text{d}), & \dfrac{\max(\rho)}{\min(\rho)} \le MDCR \end{cases} \\ &\text{with : } \begin{cases} \rho = \{\rho_0, \rho_1, \ldots, \rho_M\} \\ k = 1, 2, \ldots, M. \end{cases} \end{aligned} \tag{30}$$

The proposed SPWM-based OMTHD optimization problem is defined by (30), which consists of one single objective fitness function with a total of M_ρ (9) design variables (the DCR set), two independent parameters (N and m_T), and a set of four constraints, defined by (30a)–(30d), and detailed as follows:

1) (30a) sets the constraint for the desired MI value.
2) (30b) sets the normalization constraints of the DCRs.
3) (30c) sets the domain for the DCRs.
4) (30d) sets the constraint for the Maximum allowed DCR (MDCR) [7], which is the ratio between the maximum DCR value and the minimum DCR value.

The MDCR limits the allowed variation among the different voltage levels of the MLI. By restricting the MDCR, only practical DCR values are permitted, which helps to maintain the power balance between different components. The MDCR (in p.u.) may be set to any value from 1.0 (forcing EVS configuration) and up to infinity (MDCR restriction is lifted), however, a value of 10 is considered here for practical use, which is close to that of an asymmetrical CHBs with DCR set of 1:3:9 [10]. For example, assuming a DCR set of $\rho = \{0.05, 0.15, 0.3, 0.5\}$, in a 400-V nine-level CHB (corresponding to a 10 V : 30 V : 60 V : 100 V dc source arrangement), then the actual MDCR will be: $\max(\rho)/\min(\rho) = 0.5/0.05 = 10$.

B. Theoretical SPWM OMTHD Results and Discussion

The proposed THD expression (18) along with the optimization problem (30) were programmed as a MATLAB script and used for obtaining the optimum DCR sets for different values of N and m_T ($4 \le N \le 31$, $0.1 \le m_T \le 1$) by utilizing the genetic algorithm process [23]. The results, including the actual MDCR values, and the %-Gain value

$$\text{Gain} = 100 \cdot \frac{\mathrm{THD_{EVS}} - \mathrm{THD_{UVS}}}{\mathrm{THD_{EVS}}} \tag{31}$$

which quantifies the THD improvement over the conventional EVS-based SPWM (under similar values of N and m_a), were summarized and are available at the following online link: https://bit.ly/SPWMSUP, along with the preprogrammed MATLAB/Maple THD functions. The obtained optimum DCRs were also utilized as static lookup tables (LUTs) for the UVS-based SPWM digital controllers for the simulation and C-HIL experimental models.

THD results of conventional LS-SPWM for $4 \le N \le 10$ and $N = 31$ (with MDCR ≤ 10) are shown in Fig. 6(a), while results for the proposed UVS-based OMTHD are shown in Fig. 6(b). As can be noticed in Fig. 6, the conventional EVS-based results are significantly higher and exhibit fluctuations, especially in the lower end of the MI ($m_a < 0.3$). For some lower MI ranges, EVS-based THD results of higher N values are higher than those of lower N values, as indicated in Fig. 6(a) in the encircled areas. These anomalies, and fluctuations, which are completely absent in the proposed UVS-based optimal THD results, were also confirmed using conventional spectra-based numerical calculations, thus they cannot be attributed to any calculation errors. Unlike the conventional approach, the proposed UVS-based approach exhibits a smoother and more "analytical" behavior, with the most noticeable THD improvement occurring at the lower MI range ($m_a < 0.5$).

The corresponding actual MDCR results and the calculated %-Gain (improvement) are presented in Fig. 7(a) and (b), respectively. All actual MDCR values remain restricted to the preset constraint of 10 [see Fig. 6(a)]. As it can be concluded from Fig. 6(b), which also indicates the average %-Gain results across the entire MI range per each N value, the higher the N value and the lower the target MI value, the better the obtained improvement. As per the results of Fig. 6(b), assuming a cutoff %-Gain of at least 30%, then the proposed OMTHD is beneficial for target MI values of up to $m_a = 0.3$, $m_a = 0.55$, and $m_a = 0.65$, for MLIs with $N = 4$, $N = 7$, and $N = 31$, respectively. At $m_a = 0.1$, the theoretical EVS-based THD results were between 232% ($N = 5$) and 40.3% ($N = 31$), while for the proposed UVS-based OMTHD, they were between 52% ($N = 5$) and 7.81% ($N = 31$). This indicates an improvement gain of up to 81%. At the higher end of the MI, the differences between the conventional EVS approach and the proposed UVS approach were more subtle with a 1% and 3% gain for ($N = 5$) and ($N = 31$), respectively. At a medium MI target of $m_a = 0.5$, the improvement was 10% and 40% for $N = 5$ and $N = 31$, respectively, which is still significant.

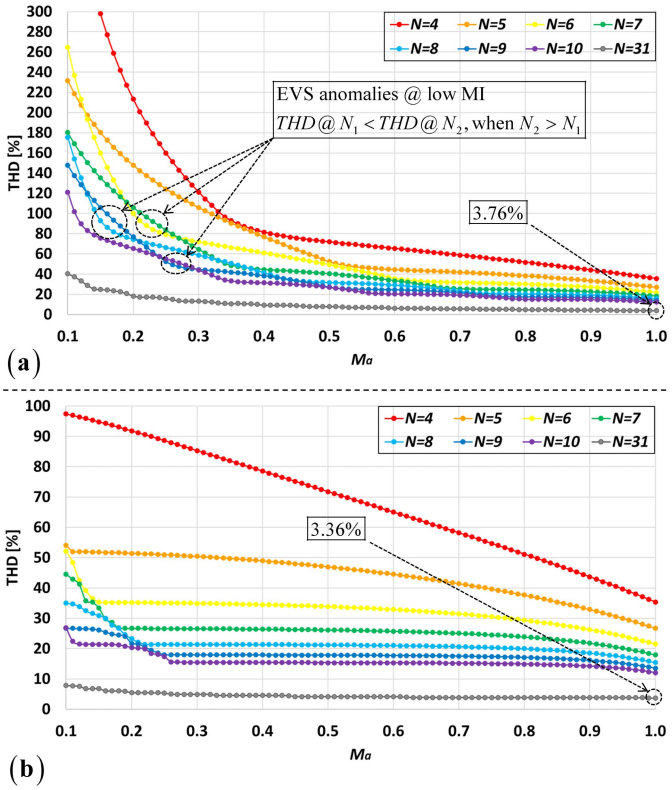

Fig. 6. Theoretical THD versus MI results for $4 \leq N \leq 31$. (a) Conventional EVS-based THD. (b) Proposed UVS-based OMTHD.

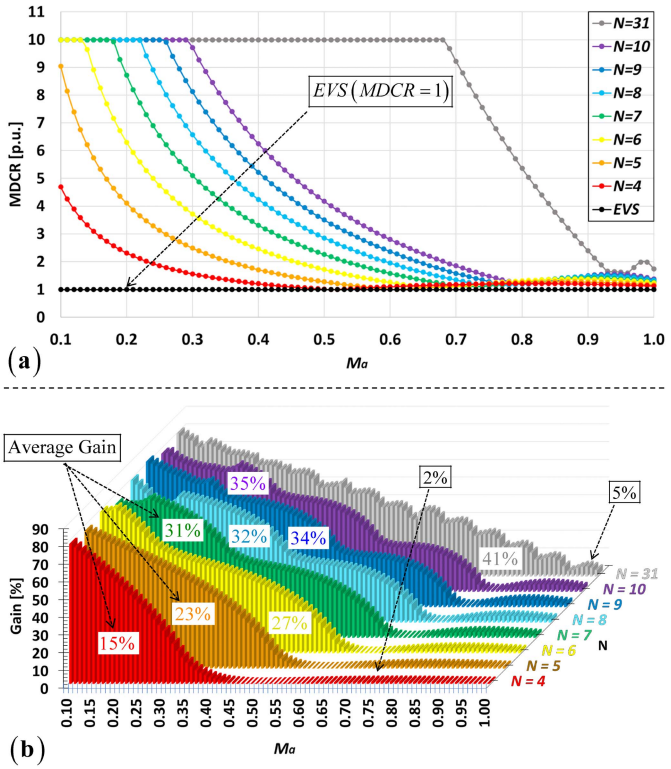

Fig. 7. Theoretical OMTHD versus MI results for $4 \leq N \leq 31$ (MDCR $\leq$ 10). (a) Calculated MDCR values. (b) Calculated %-Gain values [see (31)].

Comparisons of theoretical THD results for the seven-level case are presented in Fig. 8, along with zoomed-in sections

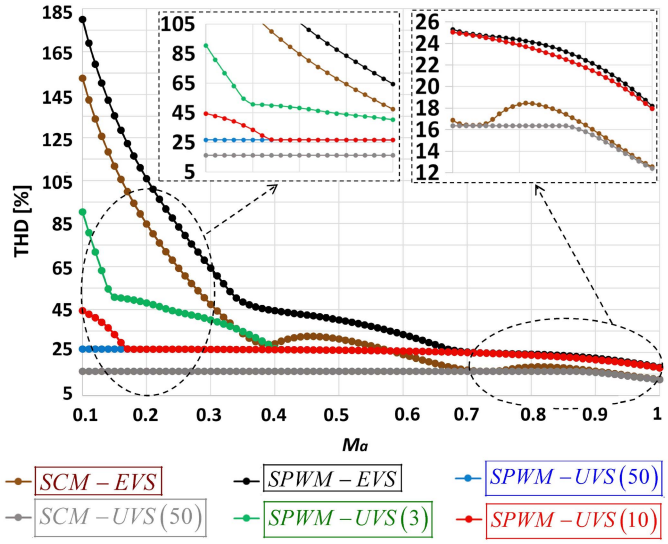

Fig. 8. Comparison of theoretical THD versus MI results for $N = 7$, from different methodologies and conditions, such as EVS- and UVS-based SCM [7], and SPWM with different MDCR restrictions (indicated in brackets).

TABLE I

THD PERFORMANCE RESULTS FOR DIFFERENT OPTIMIZATION METHODS AND DIFFERENT CONDITIONS (MDCR RESTRICTION, MI RANGE, N)

Method	Low m_a Low N	Low m_a High N	High m_a Low N	High m_a High N
SCM-EVS	Poor	Fair	Excellent	Excellent
SCM-UVS (Wide)	Good	Excellent	Excellent	Excellent
SPWM-EVS	Poor	Poor	Good	Excellent
SPWM-UVS (Tight)	Poor	Poor	Good	Excellent
SPWM-UVS (Normal)	**Fair**	**Good**	**Good**	**Excellent**
SPWM-UVS (Wide)	Fair	Excellent	Good	Excellent

for the lower and higher MI regions. The THD results of the proposed SPWM-based OMTHD, obtained for three different MDCR restrictions, were compared against three other methodologies: 1) EVS-based SPWM; 2) EVS-based SCM OMTHD [7]; and 3) UVS-based SCM OMTHD, obtained using the method from [7] (MDCR $\leq$ 50). The MDCR restrictions used for the SPWM-based OMTHD, were: 1) Normal (MDCR $\leq$ 10); 2) Wide (MDCR $\leq$ 50); and 3) Tight (MDCR $\leq$ 3). While the results in Fig. 8 are for the representative case of $N = 7$, the conclusions presented here were drawn from observations, obtained by repeating the analysis from Fig. 8 using three additional values of N in the range of $5 \leq N \leq 31$ (not shown here for the sake of brevity).

The categorization of voltage THD performance, obtained using different methods and conditions, is summarized in Table I. The performance scores were determined based on the IEEE 519 standards for line-voltage THD limits [21, Table]. This was achieved by dividing the calculated phase-voltage THD of the single-phase MLI by 3, as per conclusions made for the EVS case in [22]. The performance scores were grouped into four possible categories, which were determined as follows: "Excellent" if THD/3 $\leq$ 5%; "Good" if THD/3 $\leq$ 8%; "Fair" if THD/3 $\leq$ 10%; and "Poor" if THD/3 $\leq$ 15%, where THD indicates the single-phase voltage THD.

The THD of an SPWM waveform cannot compete with the THD of an SCM waveform, which is free from any

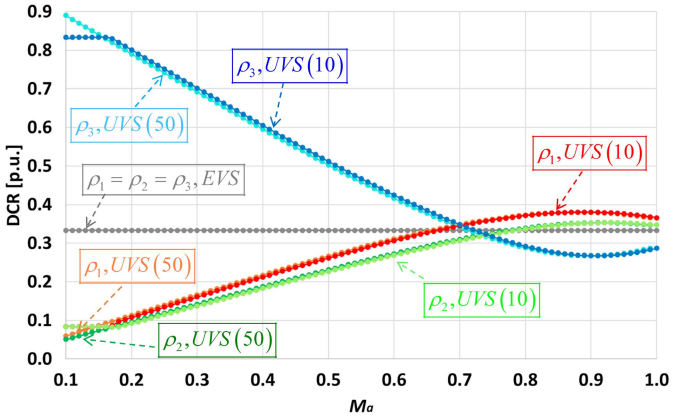

Fig. 9. Seven-level optimum DCR results of the proposed SPWM-based OMTHD: MDCR $\leq$ 10 versus MDCR $\leq$ 50.

high switching frequency harmonic components. Additionally, UVS-based SCM utilizes twice as much optimization capability, since both the SAs and DCRs serve as optimizable design variables, compared to only the DCRs in SPWM. Still, as per the results in Table I, the THD performance of the proposed UVS-based SPWM approach is quite attractive, especially when compared to conventional EVS-based SPWM or SPWM methods. The overall averaged THD performance from best to worst was as follows: 1) UVS-based SCM; 2) UVS-based SPWM with Wide MDCR restriction; 3) UVS-based SPWM with Normal MDCR restriction; 4) EVS-based SCM; 5) UVS-based SPWM with Tight MDCR restriction; and 6) nonoptimized EVS-based SPWM. These results correlate with those in Figs. 6 and 7.

Theoretical results of the optimum DCR sets obtained for the proposed OMTHD, using MDCR restrictions of 10 (normal) and 50 (wide) are presented in Fig. 9 for the seven-level case. The DCR values of the conventional EVS-based SPWM case are also included for reference. The EVS-based DCRs, which are constant, and given by (10), constitute the UVS-based DCRs' average values of the MI. It can be noted in Fig. 9 that the higher the MI value, the lower the DCRs' variability, which explains the behavior of the %-Gain (31) results in Fig. 7(b). It should be indicated that since for $N = 3$, there is no room for optimization, as $M_\rho = 1$ (only one DCR variable is available, which must be set to 1.0 to ensure $m_a = 1.0$).

IV. Validation

A. Practical Considerations for UVS-Based DC Supply

While the topic of asymmetric dc supply generation for MLIs is somewhat out of scope for this theoretical research, some design considerations and discussion of possible challenges and limitations should be briefly addressed before simulation and experimental validation are introduced.

A UVS-based MLI requires that the normalized DCR values be scaled by a factor of $V_{dc}/2$, to make up the dc source of each level, according to the MLI's topology, as generally illustrated in Fig. 2 [7], [24]. While a UVS-based arrangement may be obtained for NPC using an active frontend solution [8], [24], such practice is much more challenging, compared to the more popular CHB topology, which may utilize asymmetric

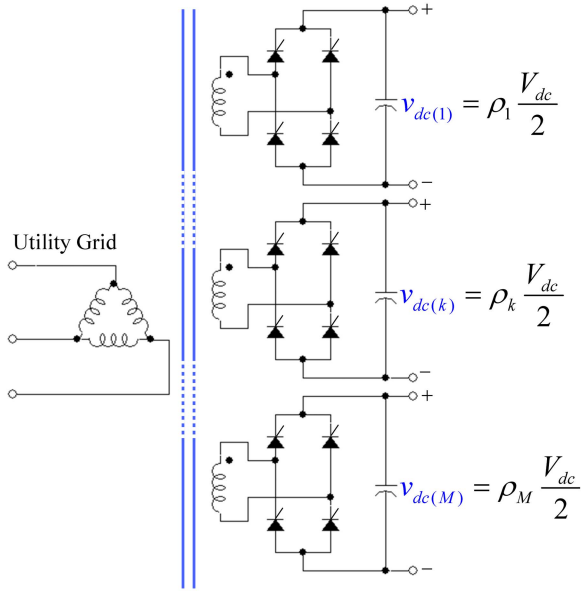

Fig. 10. Implementation example of dc Supply for UVS-based CHB MLIs.

isolated dc sources to ensure UVS-based operation. Another CHB topology advantage over the NPC is its ability to tackle faulty modules by implementing a fail-safe control algorithm in which the failed CHB cell is detected, and bypassed by auxiliary switches while loading an alternative modulation scheme for the remaining active modules [6]. For example, a three-cell, seven-level MLI with one bypassed module, could still serve as a two-cell UVS-based MLI with a five-level THD optimization. However, both power balance and fault handling are far beyond the scope of this preliminary research. This is why, for sake of brevity, a simple seven-level CHB is utilized here for the verification process, without loss of generality [7].

One popular approach to asymmetric CHB voltage supply utilizes a low-frequency multiwinding transformer and isolated SCR-based controlled rectifiers, as suggested in [9] and [24], and illustrated in Fig. 10. The other and more advanced approach utilizes a medium-frequency transformer and separate dc–dc converters, which ensures better performance (lower voltage ripple and better control dynamic), as suggested in [25].

It should be indicated that in conventional EVS-based MLIs, employing the popular LS-SPWM approach, unequal distribution of the PWM signals among the various CHB cells, which results in uneven power distribution among the CHB cell, can be compensated by DSP through a cyclic redistribution or a sorting algorithm of the switching signals among all M cells [26], [27]. While technically feasible, such power-sharing balance techniques are challenging to apply in UVS-based MLIs, because the cells' voltage supply must be redistributed to follow the PWM control signals to maintain synchronization with the corresponding DCRs. Such a practice would result in a more complex system and increased overall cost [19], [24].

B. Simulation-Based Verification

In Section III-A, it was shown that conventional EVS-based SPWM, exhibits significantly higher THD than the

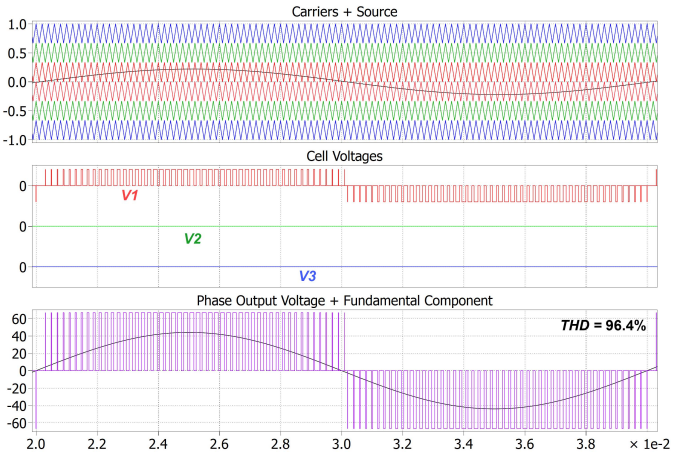

Fig. 11. EVS-based simulation results ($m_a = 0.22$): $N = 7$ ($N_{\text{eff}} = 3$).

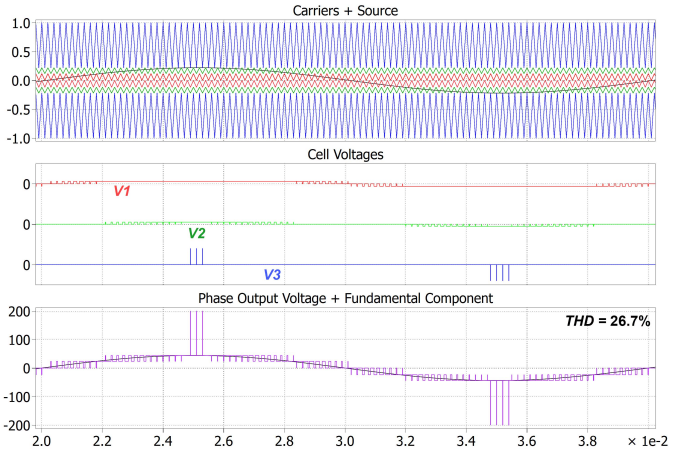

Fig. 12. UVS-based simulation results ($m_a = 0.22$): $N = 7 (N_{\text{eff}} = 7)$.

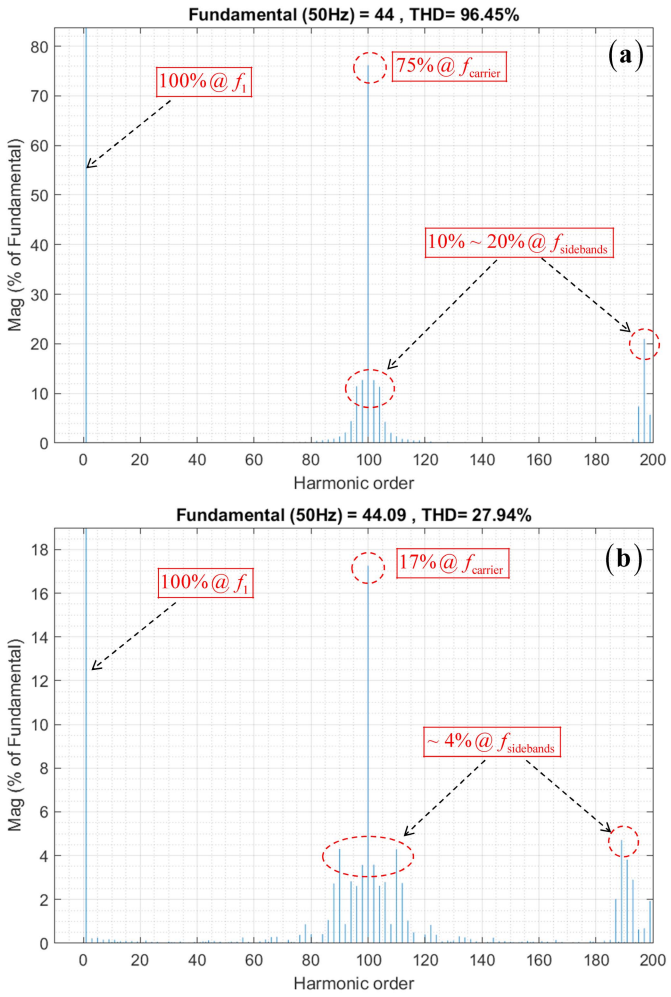

Fig. 13. FFT Spectrum of simulation results ($m_a = 0.22$). (a) Conventional EVS-based SPWM. (b) Proposed UVS-based SPWM.

proposed UVS-based SPWM, fluctuations along the MI range, and may even exhibit some anomalies, in which higher N values may contribute to higher THD values, instead of lower. By reviewing the waveforms of the simulation results in Figs. 11 and 13 ($V_{\text{dc}} = 400$ V, $f_{\text{sw}} = 5$ kHz, $f_1 = 50$ Hz) and their corresponding FFT spectrum in Fig. 12, the mechanism of such THD discrepancies and waveform anomalies can be identified. As the MI is reduced from its nominal value of $m_a = 1.0$, which is the highest linear modulation, the effective value of output voltage level count, N_{eff}, is also reduced from its nominal value, N, resulting in higher THD, fluctuations, and the aforementioned anomalies due to less effective utilization of the available N voltage steps.

For example, SPWM simulation results with $m_a = 0.22$ are shown in Figs. 11 and 12, for seven-level EVS and UVS cases, respectively. These waveforms include (top to bottom): the source and carrier signals, the cell output voltages of the CHB MLI, and the resulting output voltage, in which the measured THD and the N_{eff} value is also indicated. Note that the $N - 1$ symmetric (positive and negative) carrier signals are associated with a specific level, which is indicated by matching color coding in Figs. 11 and 12. As can be concluded from Figs. 11 and 12, not all carrier signals contribute equally to the total SPWM generation. This means that for lower MI values, some CHB cells may remain completely inactive, such as V_2 and V_3 in Fig. 11. This leads to a reduction in the effective voltage level count, N_{eff}, as the MI value is lowered, consequently, to a higher THD compared to the proposed UVS-based approach, in which such problems are eliminated, resulting in an improved THD. The significant improvement in THD performance in the proposed strategy can also be explained by comparing the FFT spectrum of the conventional EVS-based strategy with that of the proposed UVS-based strategy, as illustrated in Fig. 13 for the same low MI value of $m_a = 0.22$. The FFT spectra comparison in Fig. 13 reveals the significant reduction in the higher harmonic energy for the proposed approach compared to the conventional approach. In the UVS-bases approach, the dominant carrier harmonic magnitude is reduced by 58%, while for the dominant sideband harmonics, the magnitudes are reduced by roughly 16% compared to the EVS-based approach. This leads to a THD reduction from 96% to 27% (see Figs. 11 and 12).

As can be noticed in the results in Figs. 11 and 12, even at the very low MI of 0.22, the proposed UVS-based OMTHD still utilizes all of the seven available voltage levels, with $N_{\text{eff}} = N = 7$ (full-rank level utilization), and a THD of ~27%, which constitutes a 72% improvement gain.

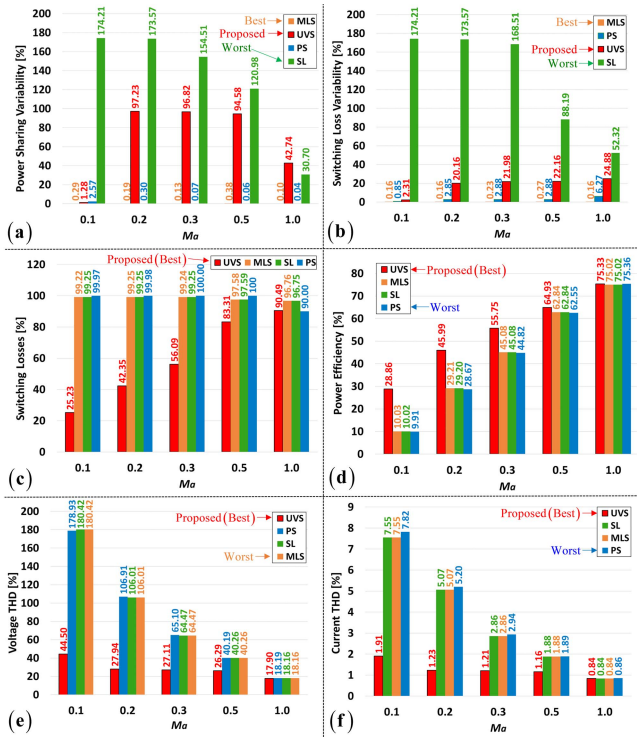

Fig. 14. Comparison of key performance parameters: proposed UVS-based SPWM method versus other SPWM methods, using seven-level CHB MLI simulations. (a) Power sharing variability. (b) Power efficiency. (c) Normalized switching losses. (d) Switching losses variability. (e) Voltage THD. (f) Load current THD.

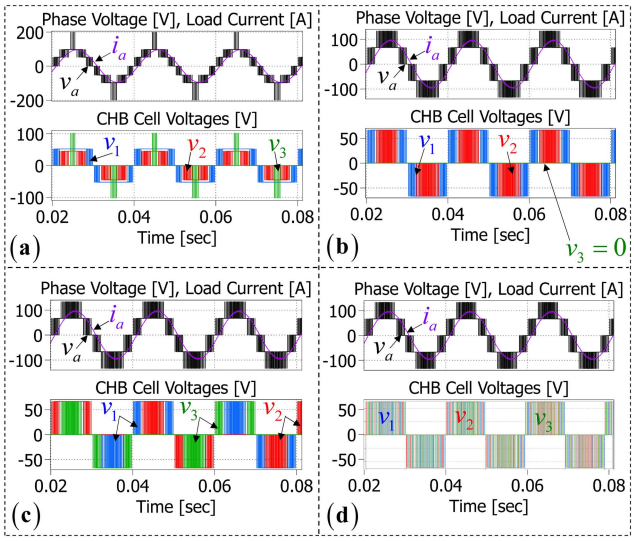

Fig. 15. Waveforms of simulation results of seven-level CHB ($m_a = 0.5$) with the different SPWM method. (a) UVS. (b) LS. (c) MLS. (d) PS.

Simulations of a seven-level *RL*-loaded CHB, operated using the following SPWM methods: 1) the novel optimized method (UVS); 2) the LS-SPWM method (LS); 3) the PS-SPWM method (PS); and, 4) the Modified LS-SPWM method (MLS), were repeated with different MI values and then analyzed for key performance parameters, which are presented in Fig. 14. The corresponding simulation waveforms for the $m_a = 0.5$ case are depicted in Fig. 15. Matching following conditions were used for all simulations: $V_{\text{dc}} = 400$ V, $f_{\text{sw}} = 3$ kHz, $f_1 = 50$ Hz, $R = 10\ \Omega$, $L = 10$ mH.

The MLS method utilized a sorting algorithm to rotate the PWM signals among the CHB cells, to maintain power balance [27]. The PS method does not require power balancing, as it is an intrinsic feature of PS-SPWM [16].

The performance parameters included in the comparison, are as follows: first, power sharing and switching loss variabilities, which, are shown in Fig. 14(a) and (b), respectively. The variability parameters are simply coefficients of variation (standard deviation to average ratio, in percent). They indicate how much power each cell delivers to the load and how much power is lost in each cell that makes up the seven-level, three-cell CHB; second, total switching losses and power efficiency (in percent), which are shown in Fig. 14(c) and (d), respectively; and, third, voltage and load current THDs, which are shown in Fig. 14(e) and (f), respectively. To ensure similar operating conditions for all of the compared SPWM methods, the carrier frequency (f_c) for all methods was set to 3 kHz, except for the PS-SPWM method, in which the carrier frequency was set to 500 Hz, which is exactly a $1/(N-1) = 1/(7-1) =$ $1/6$ fraction of the actual switching frequency, as required for a PS-SPWM [9]. The power loss analysis was carried out separately for switching and conduction losses, by using the PSIM[1] IGBT thermal module in a Simulink-PSIM cosimulation. It should be indicated that unlike switching losses, which are sensitive to the chosen SPWM method, conduction losses are only affected by the load current and the MLI topology, which were the same (conduction losses showed no noticeable cell-to-cell or method-to-method variation).

As the results in Fig. 14 reveal, while the MLS method has the best overall power sharing, the proposed UVS method has excellent power sharing and loss variations performance at low MI values, and the best overall power efficiency due to the lowest switching losses, especially at the low and medium MI range. This is due to the better utilization of all voltage levels (CHB cells), as the results in Fig. 15 indicate. In the novel UVS approach, none of the CHB cells become inactive at lower MI, which contributes to better power sharing and efficiency (see Fig. 15). The proposed UVS method also has the best harmonic performance across the entire MI range, for voltage THD, as well as load current THD, as Fig. 14(e) and (f) indicate.

The proposed method was also compared to the simulation results of other methods, which were reported by other researchers. The comparison results are summarized in Table II. The results include the number of voltage levels, N, the carrier frequency, f_c, the source, the SPWM method, the voltage THD and current THD (THD-I) results (obtained by simulation with the same load and test conditions), and the MDCR value. The MDCR was 1.0 for all EVS-based conventional methods, while never exceeding a value of 10 for the proposed UVS-based method. As the results in Table II reveal, the proposed UVS method has the lowest voltage and current THD results with %-Gains that vary from 14% to 86% for voltage THD, and from 1.84% to 68% for current THD,

[1]Trademarked.

TABLE II
FFT-BASED THD ANALYSIS: UVS VERSUS OTHER METHODS

#	N	m_a	f_c (Hz)	Source	SPWM	THD (%)	THD-I (%)	MDCR (p.u.)
1	7	1.0	1000	Ref [13]	LS	17.92	2.43	1.00
				Proposed	**UVS**	**17.59**	**2.08**	**1.27**
2	11	1.0	10000	Ref [14]	LS	11.38	2.88	1.00
				Proposed	**UVS**	**10.82**	**1.38**	**1.41**
3	11	0.2	10000	Ref [14]	LS	55.38	13.02	1.00
				Proposed	**UVS**	**17.86**	**2.24**	**10.0**
4	13	0.1	450	Ref [15]	PS	109.70	0.65	1.00
				Proposed	**UVS**	**18.03**	**0.19**	**10.0**
5	13	0.3	450	Ref [15]	PS	34.16	0.56	1.00
				Proposed	**UVS**	**13.09**	**0.10**	**10.0**
6	13	0.6	450	Ref [15]	PS	16.30	0.45	1.00
				Proposed	**UVS**	**11.35**	**0.06**	**4.23**
7	7	0.9	10	Ref [16]	LS-PS	20.70	0.44	1.00
				Proposed	**UVS**	**20.15**	**0.28**	**1.85**

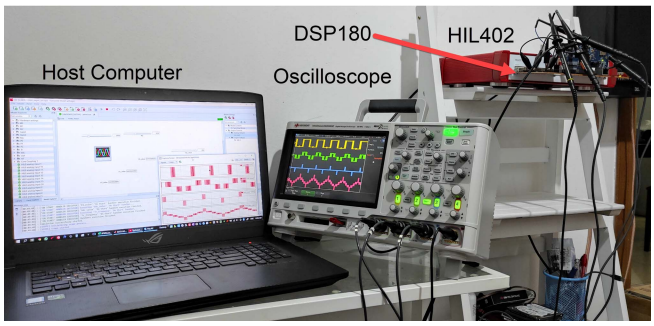

Fig. 16. C-HIL-based experimental setup.

regardless of the switching frequency used, which varied from 450 Hz up to 10 kHz.

C. Realtime C-HIL-Based Experimental Verification

The proposed OMTHD was validated by C-HIL-based real-time digital simulation, using the Typhoon HIL402 [28], and the DSP180 controller card (C2000-based MCU) [29], which was used to implement the SPWM controller, as depicted in Fig. 16. C-HIL-based experiments of seven-level EVS and UVS CHB MLIs were carried out and analyzed for THD using the built-it FFT analyzer of the Keysight X3014T oscilloscope. The obtained experimental waveforms compare the conventional unoptimized EVS with the novel UVS-based optimized approach, under similar test conditions ($V_{\rm dc} = 400$ V, $f_{\rm sw} = 5$ kHz, $f_1 = 50$ Hz), for medium-low MI of $m_a = 0.42$ and a medium-high MI of $m_a = 0.9$, are presented in Figs. 17 and 18, respectively, for both the conventional LS-SPWM EVS and novel UVS-based SPWM, separately. The results, which include (top to bottom) the three cell voltages and the output voltage, are presented in Figs. 17(a) and 18(a) for the EVS cases, and in Figs. 17(b) and 18(b), for the proposed UVS cases, respectively.

As can be learned from Fig. 17, the measured THD results match the theoretical (calculated) THD results. The $N_{\rm eff}/N$ ratio and the FFT-based voltage THD results are also indicated in Figs. 17 and 18. Similar to the low-MI-based simulation results of Section IV-B, the proposed optimized approach results in significantly lower THD at medium-low MI, which also contributed to the better utilization of all available voltage levels for the novel optimized method, namely, higher $N_{\rm eff}/N$ ratio (all seven available levels are utilized in the proposed UVS approach, as opposed to only five of them utilized in conventional EVS SPWM). The THD

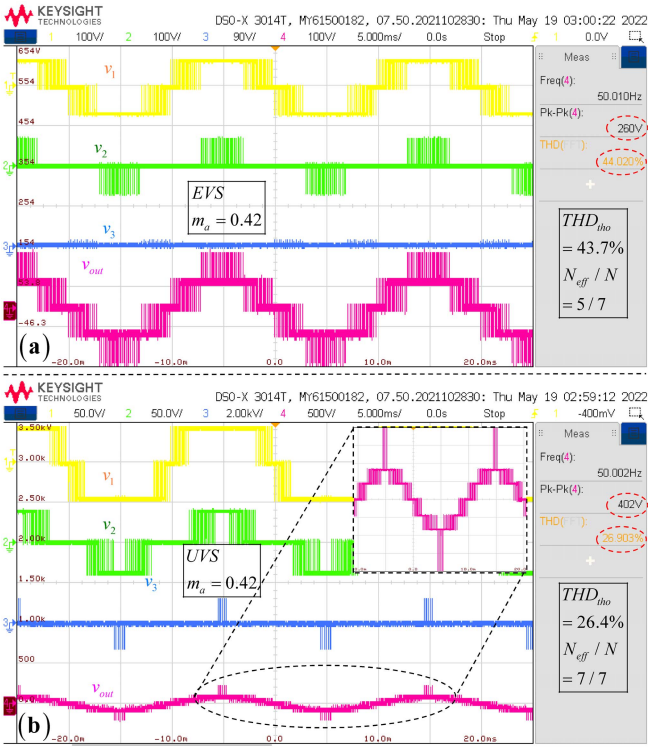

Fig. 17. Comparison of experimental results using a seven-level MLI with low-medium MI value ($m_a = 0.42$). (a) Conventional EVS. (b) Proposed UVS.

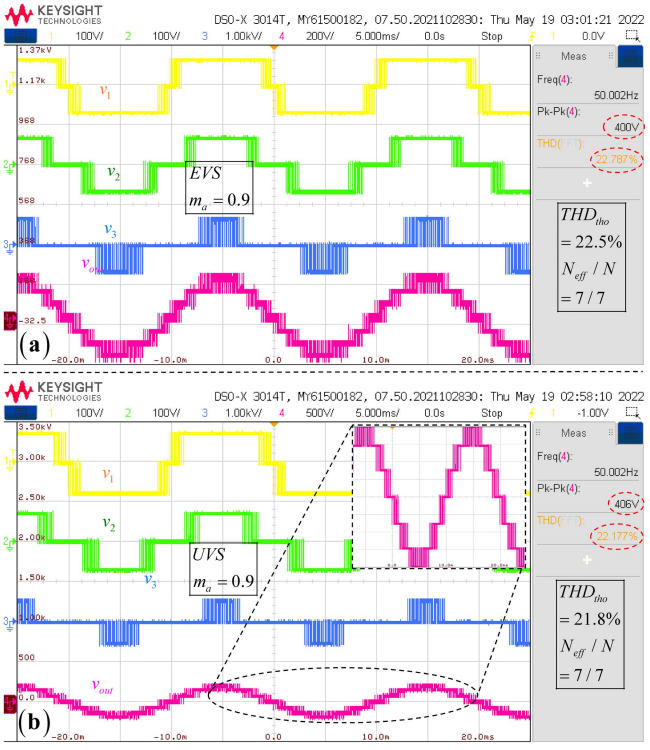

Fig. 18. Comparison of experimental results using a seven-level MLI with high MI value ($m_a = 0.9$). (a) Conventional EVS. (b) Proposed UVS.

improvement gain was 40% for $m_a = 0.42$ with an optimum DCR set of $\rho = \{0.222, 0.192, 0.586\}$, as opposed to the conventional EVS-based DCR set of $\rho = \{0.333, 0.333, 0.33\}$. For the high MI value of $m_a = 0.9$, the results, which are

presented in Fig. 18, show the expected more subtle improvement, with no difference in the N_{eff}/N ratio, thus leaving no room for significant improvement over conventional methods. The subtle improvement from 22.5% THD (EVS) to 21.8% THD (UVS) may be attributed to the optimum selection of the DCR values of $\rho = \{0.380, 0.352, 0.268\}$, which are quite close to the EVS-based DCR values of $\rho = \{0.333, 0.333, 0.33\}$. This also fully supports both the theoretical and simulation-based results from before.

V. Conclusion

In this article, a generic analytical closed-form expression of phase-voltage THD in SPWM-controlled UVS-based MLIs was derived and verified. The proposed THD formulation, which applies to both EVS- and UVS-based MLIs of any topology and any number (and parity) of voltage levels (N), was then utilized to reveal a novel SPWM-based OMTHD, in which optimum DCR are obtained using a simple single-objective fitness function. This ensures minimum THD results for any desired MI while also reducing power-sharing variability and increasing power efficiency, especially for the low and medium MI ranges. The proposed novelty was then validated by both digital simulations and C-HIL-based experiments, in which the optimization approach was implemented in a real-world DSP solution. The overwhelming results confirmed the advantages of the proposed SPWM-based OMTHD, which demonstrated significant (up to 85%) improvement compared to conventional SPWM methods. These improvements were proven to be attributed to the better utilization of all available MLI's voltage levels, compared to the compromised voltage levels utilization in conventional EVS-based SPWM. The same approach could in the future be applied to WTHD, as well as THD and WTHD of line voltages in three-phase MLIs.

Acknowledgment

The authors gratefully acknowledge Typhoon HIL Inc. company for providing the C-HIL simulation platform.

References

[1] J. Rodríguez, J.-S. Lai, and F. Z. Peng, "Multilevel inverters: A survey of topologies, controls, and applications," *IEEE Trans. Ind. Electron.*, vol. 49, no. 4, pp. 724–738, Aug. 2002.

[2] L. G. Franquelo, J. Rodriguez, J. I. Leon, S. Kouro, R. Portillo, and M. A. M. Prats, "The age of multilevel converters arrives," *IEEE Ind. Electron. Mag.*, vol. 2, no. 2, pp. 28–39, Jun. 2008.

[3] J.-S. Lai and F. Z. Peng, "Multilevel converters—A new breed of power converters," *IEEE Trans. Ind. Appl.*, vol. 32, no. 3, pp. 509–517, May 1996.

[4] I. Colak, E. Kabalci, and R. Bayindir, "Review of multilevel voltage source inverter topologies and control schemes," *Energy Convers. Manage.*, vol. 52, no. 2, pp. 1114–1128, Feb. 2011.

[5] G. Grandi and A. Ruderman, *Multilevel Converters: Analysis, Modulation, Topologies, and Applications*. Basel, Switzerland: MDPI, 2019.

[6] M. Malinowski, K. Gopakumar, J. Rodríguez, and M. A. Pérez, "A survey on cascaded multilevel inverters," *IEEE Trans. Ind. Electron.*, vol. 57, no. 7, pp. 2197–2206, Jul. 2010.

[7] E. Barbie, R. Rabinovici, and A. Kuperman, "Analytical formulation and minimization of voltage THD in staircase modulated multilevel inverters with variable DC ratios," *IEEE Access*, vol. 8, pp. 208861–208878, 2020.

[8] E. Barbie, R. Rabinovici, and A. Kuperman, "Modeling and simulation of a novel active three-phase multilevel power factor correction front end—The 'Negev' rectifier," *IEEE Trans. Energy Convers.*, vol. 35, no. 1, pp. 462–473, Mar. 2020.

[9] D. G. Holmes and T. A. Lipo, *Pulse Width Modulation for Power Converters: Principles and Practice*. Hoboken, NJ, USA: Wiley, 2003.

[10] A. A. K. Arani, H. R. Zaferani, M. J. Sanjari, and G. B. Gharehpetian, "Using genetic algorithm and simulated annealing for 27-level PV inverter THD minimization," in *Proc. Smart Grid Conf. (SGC)*, Dec. 2014, pp. 1–6.

[11] J. Chen and Y. Fu, "Topology and voltage-balance control of a single-phase active neutral point clamped seven-level inverter," *IEEE J. Emerg. Sel. Topics Power Electron.*, vol. 9, no. 4, pp. 4762–4773, Aug. 2021.

[12] Y. Babkrani, A. Naddami, S. Hayani, M. Hilal, and A. Fahli, "Simulation of cascaded H-bridge multilevel inverter with several multicarrier waveforms and implemented with PD, POD and APOD techniques," in *Proc. Int. Renew. Sustain. Energy Conf. (IRSEC)*, Dec. 2017, pp. 1–6.

[13] M. Tariq, M. Meraj, A. Azeem, A. I. Maswood, A. Iqbal, and B. Chokkalingam, "Evaluation of level-shifted and phase-shifted PWM schemes for seven level single-phase packed U cell inverter," *CPSS Trans. Power Electron. Appl.*, vol. 3, no. 3, pp. 232–242, Sep. 2018.

[14] A. M. M. Hassan, X. Yang, A. I. M. Ali, T. A. Ahmed, and A. M. Azmy, "A study of level-shifted PWM single-phase 11-level multilevel inverter," in *Proc. 21st Int. Middle East Power Syst. Conf. (MEPCON)*, Dec. 2019, pp. 170–176.

[15] R. Rabinovici, D. Baimel, J. Tomasik, and A. Zuckerberger, "Thirteen-level cascaded H-bridge inverter operated by generic phase shifted pulse-width modulation," *IET Power Electron.*, vol. 6, no. 8, pp. 1516–1529, Sep. 2013.

[16] S. Rahman, M. Meraj, A. Iqbal, B. Prathap-Reddy, and I. Khan, "A combinational level shifted and phase shifted PWM technique for symmetrical power distribution in CHB inverters," *IEEE J. Emerg. Sel. Topics Power Electron.*, early access, Aug. 9, 2021, doi: 10.1109/JESTPE.2021.3103610.

[17] J. Soomro, E. A. Qasmi, F. A. Chachar, J. A. Ansari, and S. A. Soomro, "Comparative analysis of level shifted PWM techniques for conventional and modified cascaded seven level inverter," in *Proc. Int. Conf. Comput., Math. Eng. Technol. (iCoMET)*, Mar. 2018, pp. 1–6.

[18] V. S. K. Devi and S. G. Srivani, "Modified phase shifted PWM for cascaded H bridge multilevel inverter," in *Proc. 3rd Int. Conf. Adv. Electr., Electron., Inf., Commun. Bio-Inform. (AEEICB)*, Feb. 2017, pp. 89–94.

[19] M. Meraj, S. Rahman, A. Iqbal, and N. Al Emadi, "Novel level shifted PWM technique for unequal and equal power sharing in quasi Z-source cascaded multilevel inverter for PV systems," *IEEE J. Emerg. Sel. Topics Power Electron.*, vol. 9, no. 1, pp. 937–948, Feb. 2021.

[20] A. K. Ranjan, D. V. Bhaskar, and N. Parida, "Analysis and simulation of cascaded H-bridge multi level inverter using level-shift PWM technique," in *Proc. Int. Conf. Circuits, Power Comput. Technol. (ICCPCT)*, Mar. 2015, pp. 1–5.

[21] *IEEE Recommended Practice and Requirements for Harmonic Control in Electric Power Systems*, IEEE Standard 519-2014 (Revision of IEEE Standard 519-1992), Jun. 2014, pp. 1–29.

[22] A. Ruderman, B. Reznikov, and S. Busquets-Monge, "Asymptotic time domain evaluation of a multilevel multiphase PWM converter voltage quality," *IEEE Trans. Ind. Electron.*, vol. 60, no. 5, pp. 1999–2009, May 2013.

[23] Y. Tao, B. Li, T. Dragicevic, T. Liu, and F. Blaabjerg, "HVDC grid fault current limiting method through topology optimization based on genetic algorithm," *IEEE J. Emerg. Sel. Topics Power Electron.*, vol. 9, no. 6, pp. 7045–7055, Dec. 2021.

[24] E. Barbie, D. Baimel, and A. Kuperman, "Frequency spectra based approach to analytical formulation and minimization of voltage THD in staircase modulated multilevel inverters," *Alexandria Eng. J.*, vol. 61, no. 10, pp. 7781–7809, Oct. 2022.

[25] Y.-K. Tran and D. Dujic, "A multiport medium voltage isolated DC–DC converter," in *Proc. 42nd Annu. Conf. IEEE Ind. Electron. Soc.*, Oct. 2016, pp. 6983–6988.

[26] I. Sarkar and B. G. Fernandes, "Modified hybrid multi-carrier PWM technique for cascaded H-bridge multilevel inverter," in *Proc. 40th Annu. Conf. IEEE Ind. Electron. Soc.*, Oct. 2014, pp. 4318–4324.

[27] J.-M. De Paris, C. R. D. Osorio, H. Pinheiro, and F. D. M. Carnielutti, "Phase disposition modulation with sorting algorithm for symmetrical cascaded multilevel converters," *IEEE Trans. Ind. Appl.*, vol. 55, no. 6, pp. 7527–7536, Nov. 2019.

[28] *Typhoon HIL402 Bochure*. Accessed: Nov. 16, 2022. [Online]. Available: https://www.typhoon-hil.com/doc/products/Typhoon-HIL402-brochure.pdf

[29] *DSP180 Brochure*. Accessed: Nov. 16, 2022. [Online]. Available: https://www.typhoon-hil.com/doc/brochures/HIL-DSP-180-Interface.pdf